RESEARCH

Breaking the left-right symmetry in fluttering artificial cilia that perform nonreciprocal oscillations

Ariel Surya Boiardi · Roberto Marchello

Abstract Recent investigations on active materials have introduced a new paradigm for soft robotics by showing that a complex response can be obtained from simple stimuli by harnessing dynamic instabilities. In particular, polyelectrolyte hydrogel filaments actuated by a constant electric field have been shown to exhibit self-sustained oscillations as a consequence of flutter instability. Owing to the nonreciprocal nature of the emerging oscillations, these *artificial cilia* are able to generate flows along the stimulus. Building upon these findings, in this paper we propose a design strategy to break the left-right symmetry in the generated flows, by endowing the filament with a natural curvature at the fabrication stage. We develop a mathematical model based on morphoelastic rod theory to characterize the stability of the equilibrium configurations of the filament, proving the persistence of flutter instability. We show that the emerging oscillations are nonreciprocal and generate thrust at an angle with the stimulus. The results we find at the level of the single cilium open new perspectives on the possible applications of artificial ciliary arrays in soft robotics and microfluidics.

1 Introduction

Cilia are tiny active filaments ubiquitous in living systems, from single cell organisms to mammalian epithelial tissue. Both isolated, as is the case of *flagella*, or assembled in complex *ciliary carpets*, cilia serve a variety of functions, such as sensing [1], locomotion [2, 3], fluid motion [4] and transport [5]. The effectiveness of these structures in carrying out such a wide range of tasks has inspired the development of artificial replicas for biomimetic actuators, with possible applications in micro-robotics.

While self-sustained oscillations in biological cilia are realized internally by complex molecular motors [6], various external actuation principles have been proposed for artificial cilia, depending on the technologies and materials employed, such as light driven liquid crystals [7], electrically [8] and acoustically [9] actuated hydrogels, and a variety of magnetically responsive materials [10, 11]. Notably, in all mentioned examples, self-sustained oscillations were achieved by spatial or temporal modulation of the external stimuli.

Ariel S. Boiardi and Roberto Marchello have contributed equally to this work.

A. S. Boiardi (✉) · R. Marchello
Mathematics Area, SISSA - International School for Advanced Studies, Via Bonomea 265, 34136 Trieste, TS, Italy
e-mail: aboiardi@sissa.it

R. Marchello
e-mail: roberto.marchello@sissa.it

Recent studies have proposed solutions to overcome this limitation by harnessing mechanical instabilities as a way to generate a time dependent response from a steady stimulus. Along this research line, notable examples comprise passive filaments driven by Quincke rotation [12], photoactive filaments exploiting the self-shadowing mechanism proposed in [13], and the emergence of flutter instability in polyelectrolyte (PE) hydrogels, as shown in [14]. An intriguing perspective on this approach comes from the natural world, where instabilities have been found to be responsible for many complex emergent behaviours: from flagellar beating [15, 16] to plants circumnutations [17–19].

As for the work in [14], experiments on PE gel filaments have provided evidence that self-sustained, periodic oscillations can be achieved by means of a steady and uniform electric field, a behaviour that was interpreted as an instance of flutter instability emerging from the filament's activity and its interaction with the viscous environment. Interestingly, the arising cyclic motion of such filaments is nonreciprocal, and indeed causes a net thrust in the surrounding fluid in the direction of the electric field, as shown in the left panel of Fig. 1.

Left-right (LR) symmetry breaking is an important function carried out by specialized ciliate cells during mammal embryo development [20]. Drawing inspiration from Nature, the possibility to generate and control complex fluid flows in lab-on-a-chip devices has become a prevalent research field. As shown in the central panel of Fig. 1, asymmetric flows can be generated with the model of [14] by simply reorienting the electric field. Clearly, this strategy would require the modulation in space of the external stimulus to generate a target flow field from an array of artificial cilia. Instead, one might want to achieve the same result by the material and geometric design of the cilia, while keeping the external control simple. This would allow to realize a system of cilia which, under a uniform and constant stimulus, may oscillate so as to generate complex flow fields in the fluid.

In this work, we present a way to tackle this point. In particular, we extend the theoretical results of [14] by considering active filaments which are designed to be naturally curved, i. e. whose stress-free configuration is curved. Results from the present study are anticipated in the right panel of Fig. 1, showing that it is indeed possible to control the emerging dynamics of an active filament by proper design.

The manuscript is organized as follows. We introduce in Sect. 2 the mathematical model for morphoelastic filaments endowed with natural curvature and interacting with a viscous fluid in the context of low Reynolds number hydrodynamics. Section 3 is devoted to the analysis of the equilibrium configurations of such active filaments and to the characterization of their stability. Numerical experiments are presented in Sect. 4 to explore the dynamics of self-oscillating filaments in the nonlinear regime.
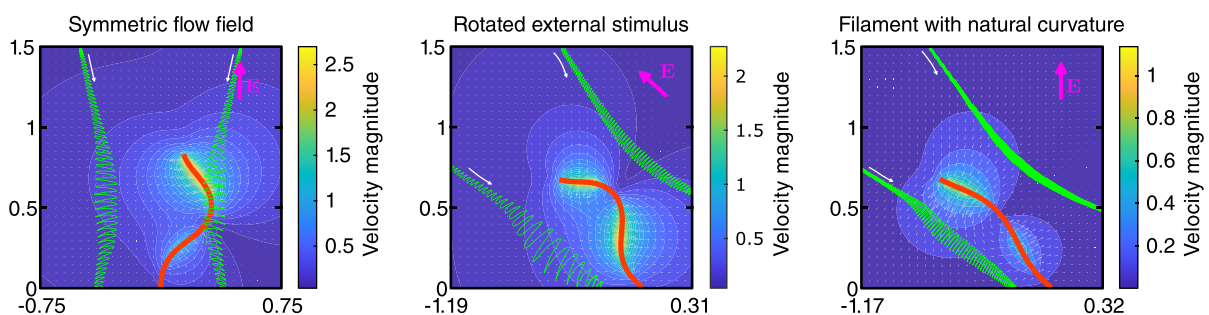
Fig. 1 Spontaneous motion of active filaments subject to a uniform and steady electric field **E** and induced fluid flow. Following the motion of massless *tracer* particles transported by the fluid flow, we get the *path lines* in green. These allow to visualize and highlight the net effect of the oscillating filament on the surrounding fluid. The case of a straight filament subject to a vertical field (left panel) corresponds to the study in [14] and is reported for comparison purposes. As the electric field is rotated (central panel), the oscillatory motion in a straight filament is at an angle with respect to the vertical line and so is the average fluid flow (see average direction of the path lines). From a qualitative standpoint, the same effect is achieved by endowing an active filament with a *natural curvature* in the fabrication stage, while keeping the electric stimulus vertical (right panel). See Appendix A for the details of the numerical simulations exploited to obtain the presented results

Section 5 closes the manuscript and presents future perspectives.

2 Mathematical model

In this section, we introduce a minimal mathematical model for an active filament with natural curvature. We describe the filament as an inextensible and unshearable rod [21] and account for its activity by exploiting the framework of morphoelastic rods [22]. Hence, the filament's activity is encoded by an internal degree of freedom, namely the *spontaneous curvature*, which constitutively depends on the external stimulus, as later detailed. Similarly to a previous study [14], the filament is clamped at one extremity and is allowed to undergo planar motions while interacting with a viscous fluid.

We fix an orthonormal basis $\{\mathbf{e}_1, \mathbf{e}_2\}$ such that the external stimulus $\mathbf{E} = E\mathbf{e}_2$ is in the direction of $\mathbf{e}_2$. Since the rod is subject to large deformation, we identify its reference configuration with a segment in the direction of $\mathbf{e}_2$ and we describe its current configuration through the motion $(s,t) \mapsto \mathbf{r}(s,t)$, parameterized in arc-length $s \in [0, L]$ and time $t \geq 0$, see Fig. 2. Defining $\theta(s,t)$ as the positive, anticlockwise angle between the tangent to the filament and $\mathbf{e}_2$, we introduce the unit tangent $\mathbf{t}(s,t)$ and the unit normal $\mathbf{n}(s,t)$ to the current configuration as

Fig. 2 Sketch of a morphoelastic filament of length L and natural curvature κ_N, clamped at its base and subject to the vertical external field $\mathbf{E}$

$$
\begin{aligned}
\mathbf{t} &= -\sin\theta\, \mathbf{e}_1 + \cos\theta\, \mathbf{e}_2, \\
\mathbf{n} &= -\cos\theta\, \mathbf{e}_1 - \sin\theta\, \mathbf{e}_2.
\end{aligned} \tag{1}
$$

Since $\mathbf{t} = \partial_s \mathbf{r}$ and $\mathbf{r}(0,t) = \mathbf{0}$, noting that $\partial_t \mathbf{t} = \mathbf{n}\, \partial_t \theta$, we can express

$$
\mathbf{r} = \int_0^s \mathbf{t}, \quad \mathbf{v} = \partial_t \mathbf{r} = \int_0^s \mathbf{n}\, \partial_t \theta, \tag{2}
$$

so that the kinematics of the filament is completely determined by θ.

The dynamics is governed by the balance equations of linear and angular momentum: neglecting inertia these read

$$
\partial_s \mathbf{C} + \mathbf{d} = \mathbf{0}, \quad \partial_s \mathbf{M} + \partial_s \mathbf{r} \times \mathbf{C} = \mathbf{0}, \tag{3}
$$

where $\mathbf{C}$ is the internal contact force, $\mathbf{M}$ is the internal bending moment, and $\mathbf{d}$ is the viscous drag force per unit length from the surrounding fluid.

Assuming low Reynolds number hydrodynamics, the viscous drag can be approximated by Resistive Force Theory (RFT) [3]. The fluid structure interaction is hence reduced to a local coupling with the filament velocity by two *resistive coefficients* $\mu_\parallel$ and $\mu_\perp$, so that

$$
\mathbf{d} = -\left[\mu_\parallel \mathbf{t} \otimes \mathbf{t} + \mu_\perp \mathbf{n} \otimes \mathbf{n}\right]\mathbf{v} = -\mu_\parallel v_\parallel \mathbf{t} - \mu_\perp v_\perp \mathbf{n}, \tag{4}
$$
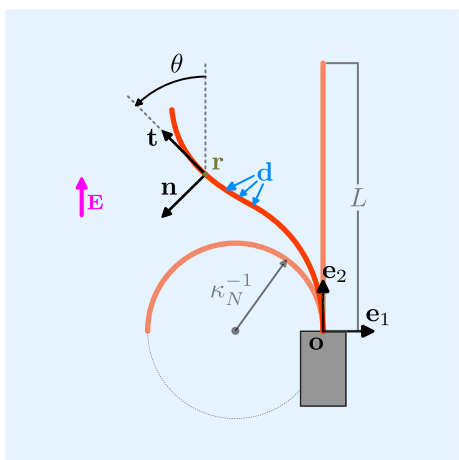
where $v_\parallel$ and $v_\perp$ are the tangent and normal components of the velocity, respectively. In the slender limit, it is known that $\mu_\perp = 2\mu_\parallel$, a relation that will be assumed next.

It is useful to express the balance equations (3) with respect to the local basis $\{\mathbf{t}, \mathbf{n}\}$. Having split the internal action in axial and shear components as $\mathbf{C} = A\mathbf{t} + V\mathbf{n}$, noting that $\partial_s \mathbf{t} = \mathbf{n}\, \partial_s \theta$ and that $\partial_s \mathbf{n} = -\mathbf{t}\, \partial_s \theta$, we can project the balance of linear momentum (3)$_1$ along $\mathbf{t}$ and $\mathbf{n}$, leading to

$$
\begin{aligned}
\partial_s A - V \partial_s \theta - \mu_\parallel v_\parallel &= 0, \\
\partial_s V + A \partial_s \theta - 2\mu_\parallel v_\perp &= 0.
\end{aligned} \tag{5}
$$

Looking back at (2)$_2$, we remark that this formulation of the balance of linear momentum is actually an integro-differential equation. Furthermore, since the problem is planar, the bending moment lies along $\mathbf{e}_3 = \mathbf{e}_1 \times \mathbf{e}_2 = \mathbf{t} \times \mathbf{n}$, i.e. $\mathbf{M} = M\mathbf{e}_3$, so that the balance of angular momentum (3)$_2$ reduces to

$$
\partial_s M + V = 0. \tag{6}
$$

For what concerns the contact force components A and V, the inextensibility and unshearability constraints prevent us from constitutively prescribing them. These are indeed reactive terms to the constraints above and need to be determined through balance equations (see [21]). We recall that the rod is modelled as morphoelastic and that it has a natural curvature κ_N, such that the constitutive law for the bending moment is

$$M = B\big(\partial_s\theta - \kappa - \kappa_N\big), \tag{7}$$

where B is the bending stiffness and $\kappa(s,t)$ is the spontaneous curvature, which encodes the active response of the filament to the external stimulus **E**. According to (7), the visible curvature $\partial_s\theta$ coincides with the sum of spontaneous and natural curvature in the absence of stress. While the natural curvature is a geometric feature introduced at the fabrication stage, the spontaneous curvature evolves according to the phenomenological law

$$\tau\partial_t\kappa + \kappa = -\kappa_E\sin\theta. \tag{8}$$

This models the viscousrelaxation with characteristic time τ to a *target curvature* κ_E, dependent on the intensity of the external stimulus modulated according to the current configuration of the filament with respect to the external field **E**. At points of the filament orthogonal to the external field, the spontaneous curvature evolves to κ_E, which is then the maximum curvature attainable by the filament at equilibrium. The value and sign of the target curvature depend on the external stimulus. In particular, κ_E is positive (negative, respectively) if E is positive (negative, respectively), and higher values of E induce higher values of κ_E. This evolution law, reminiscent of the gravitropic response of plants in the gravity field [17, 23], proves to be sufficiently accurate to describe the activity of the materials under consideration, as shown in [14] by a prototypical model. Plugging (7) into (6), the balance of angular momentum reads

$$B\big(\partial_s^2\theta - \partial_s\kappa\big) + V = 0. \tag{9}$$

The system of nonlinear equations (5), (8) and (9) is endowed with suitable boundary and initial conditions. Since the rod is clamped at the extremity $s = 0$ and has the endpoint $s = L$ free, the boundary conditions are

$$\theta(0,t) = 0,$$
$$A(L,t) = 0, \quad V(L,t) = 0, \quad M(L,t) = 0, \tag{10}$$

for any $t \geq 0$, while the initial conditions read

$$\theta(s,0) = \theta_0(s), \quad \kappa(s,0) = \kappa_0(s), \tag{11}$$

for any $s \in [0, L]$.

2.1 Nondimensional form of the governing equations

We now recast the governing equations in nondimensional form. For this purpose, we identify the length of the rod L as characteristic length and the relaxation time τ as characteristic time. Consequently we define $\bar{s} \in [0, 1]$ and $\bar{t} \geq 0$ as dimensionless independent variables such that, $s = L\bar{s}$ and $t = \tau\bar{t}$. Likewise, we rescale curvatures by L^{-1}, velocities by $L\tau^{-1}$ and forces by BL^{-2}. With a slight abuse of notation, in the following we denote dimensionless quantities by the same symbols as their dimensional counterparts. Upon introducing the three parameters

$$\eta_\| = \frac{\mu_\| L^4}{\tau B}, \quad \chi_E = L\kappa_E, \quad \chi_N = L\kappa_N, \tag{12}$$

the dimensionless governing equations are

$$\begin{aligned}
\partial_s A - V\partial_s\theta - \eta_\| v_\| &= 0, \\
\partial_s V + A\partial_s\theta - 2\eta_\| v_\perp &= 0, \\
\partial_s^2\theta - \partial_s\kappa + V &= 0, \\
\partial_t\kappa + \kappa + \chi_E\sin\theta &= 0,
\end{aligned} \tag{13}$$

where the dimensionless bending moment reads as

$$M = \partial_s\theta - \kappa - \chi_N. \tag{14}$$

Finally, the boundary conditions (10) become

$$\theta(0,t) = 0,$$
$$A(1,t) = 0, \quad V(1,t) = 0, \quad M(1,t) = 0, \tag{15}$$

for any $t \geq 0$.

3 Stability analysis

Having in mind the work in [14], where nonreciprocal periodic oscillations in gel filaments were proved to be an instance of flutter instability, we are now

interested in the stability of equilibria attained by the system governed by equations (13) and (15).

3.1 Equilibrium configurations

Since the external forces acting on the filament are of viscous nature, they are null at equilibrium. Hence, the balance of momenta together with the free-end boundary condition at $s = 1$ imply that the internal force and the bending moment vanish at equilibrium, i. e. $A_{eq} = V_{eq} = 0$, and $M_{eq} = 0$. The latter condition means that the equilibrium angle θ_{eq} must satisfy the first order differential equation $\theta'_{eq}(s) - \kappa_{eq}(s) - \chi_N = 0$ for all $s \in [0, 1]$, where the prime denotes differentiation with respect to s. On the other hand, the evolution equation $(13)_4$ gives $\kappa_{eq} = -\chi_E \sin \theta_{eq}$. Combining these relations, it is possible to determine the equilibrium configuration of the filament for different values of the angle φ at the clamp. More specifically, the equilibrium configuration is obtained by solving the following initial value problem:

$$\begin{cases} \theta'_{eq} + \chi_E \sin \theta_{eq} - \chi_N = 0 & \text{in } (0, 1], \\ \theta_{eq}(0) = \varphi, \end{cases} \tag{16}$$

where $\chi_E \in \mathbb{R}$, $\chi_N \geq 0$ and $\varphi \in [-\pi/2, \pi/2]$. The case with $\chi_N < 0$ may be easily deduced by symmetry considerations and will not be examined.

First of all, in the absence of the external stimulus, i. e. for $\chi_E = 0$, we easily get

$$\theta_{eq}(s) = \varphi + \chi_N s, \tag{17}$$

since no internal active processes take place in the rod and its equilibrium configuration is simply an arc of circle (possibly with many loops). Furthermore, if also $\chi_N = 0$, the equilibrium coincides with a straight line.

If $\chi_E \neq 0$ and $\chi_N = 0$, the integration of Eq. (16) leads to the solution

$$\theta_{eq}(s) = 2 \arctan \left[\tan \left(\frac{\varphi}{2} \right) e^{-\chi_E s} \right], \tag{18}$$

which coincides with a vertical straight line in the case of $\varphi = 0$.

If both χ_E and χ_N are not null, it is easy to show that the constant angles

$$\theta_{eq}(s) = \begin{cases} \pi/2 & \text{if } \chi_E = \chi_N, \\ -\pi/2 & \text{if } \chi_E = -\chi_N, \\ \arcsin(\chi_N/\chi_E) & \text{if } |\chi_E| > \chi_N, \end{cases} \tag{19}$$

are solutions of Eq. (16) if they are compatible with the value φ at the clamp, while there are no constant solutions if $|\chi_E| < \chi_N$. Moreover, if $\chi_E = \pm \chi_N$ the nonconstant equilibrium solutions read

$$\theta_{eq}(s) = \mp \frac{\pi}{2} + 2 \arctan \left[\tan \left(\frac{\varphi}{2} \pm \frac{\pi}{4} \right) + \chi_N s \right]. \tag{20}$$

Apart from the cases discussed above, the general solution of problem (16) reads

$$\theta_{eq}(s) = 2 \arctan \left\{ \frac{\chi_E}{\chi_N} - \sqrt{1 - \frac{\chi_E^2}{\chi_N^2}} \tan \left[-\frac{\chi_N s}{2} \sqrt{1 - \frac{\chi_E^2}{\chi_N^2}} + \arctan \frac{\frac{\chi_E}{\chi_N} - \tan \left(\frac{\varphi}{2} \right)}{\sqrt{1 - \frac{\chi_E^2}{\chi_N^2}}} \right] \right\}. \tag{21}$$

It is worth noting that, despite appearance, this function is real-valued even in the case of $|\chi_E| > \chi_N$, as can be shown by trivial trigonometric identities. Clearly, equilibrium configurations exist for $s \in [0, 1]$, but the above function is formally defined for all $s \geq 0$. In particular, it can be shown that for $|\chi_E| > \chi_N$ the limit of (21) for $s \to \infty$ exists

$$\theta_{lim} = \lim_{s \to \infty} \theta_{eq}(s) = \arcsin \left(\frac{\chi_N}{\chi_E} \right). \tag{22}$$

Having computed all the possible equilibrium angles, we now assume the boundary condition $\varphi = 0$, which is relevant to the problem at hand, and we show in Fig. 3 the corresponding equilibrium configurations for $\chi_N \in \{1, 2, 16\} \times 2\pi$ while varying $\chi_E > 0$. In the absence of the external stimulus, i. e. for $\chi_E = 0$, the filaments form 1, 2, and 16 loops, respectively. More in general, we notice that the spontaneous curvature, which is driven by χ_E, competes with the natural curvature in determining the configuration of the filaments at equilibrium. As the stimulus magnitude is increased, the filaments unwind and, for sufficiently large value of χ_E, become essentially straight and oriented as the limit angle θ_{lim}, modulo a
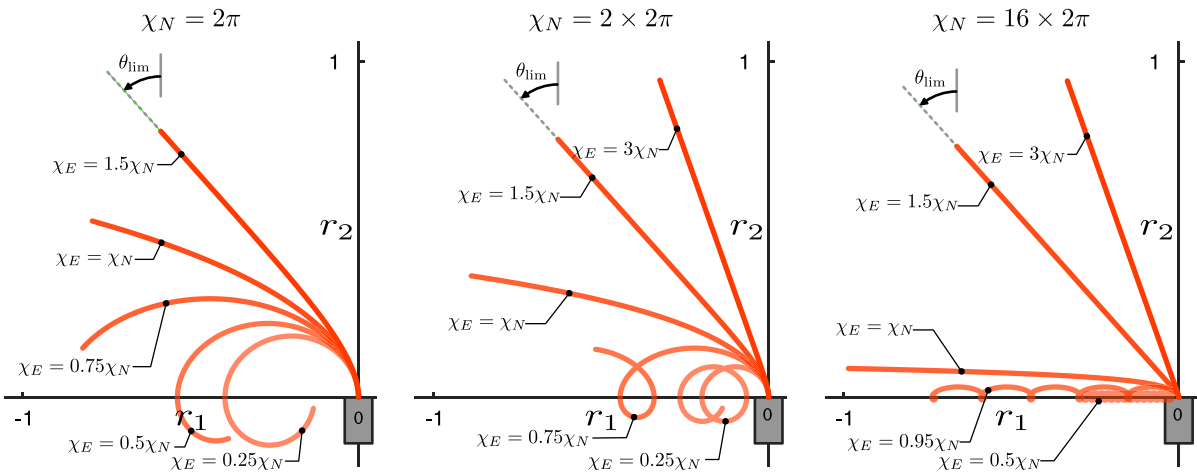
Fig. 3 Equilibrium configurations of the filament for some values of χ_N and χ_E. Since the length of the filament is normalized to 1, for $\chi_N = 2\pi$ it forms a circle in the absence of the external stimulus. Similarly, for $\chi_N = 2 \times 2\pi$ and $\chi_N = 16 \times 2\pi$ the filament forms 2 and 16 loops, respectively. The spontaneous curvature, driven by χ_E, competes with the natural curvature and has the effect of unwinding the loops and progressively straightening the filament. For sufficiently high χ_E, the filament becomes essentially straight, except for a boundary layer at the clamp, and its inclination line approximates the limit angle θ_{lim} defined in Eq. (22)

boundary layer at the clamp dictated by the boundary condition $\theta_{\text{eq}}(0) = \varphi = 0$.

3.2 Linearization about a stationary solution

In order to study the stability of the equilibrium configurations, we linearize the equations (13) assuming incremental solutions of the form

$$
\begin{aligned}
A(s,t) &= \varepsilon A^\ell(s,t), \\
V(s,t) &= \varepsilon V^\ell(s,t), \\
\theta(s,t) &= \theta_{\text{eq}}(s) + \varepsilon \theta^\ell(s,t), \\
\kappa(s,t) &= -\chi_E \sin \theta_{\text{eq}}(s) + \varepsilon \kappa^\ell(s,t),
\end{aligned}
\tag{23}
$$

being $A_{\text{eq}} = 0$, $V_{\text{eq}} = 0$ and θ_{eq} the equilibrium angle discussed in Sect. 3.1, depending on χ_E and χ_N, with $\varphi = 0$. Plugging the assumptions (23) into the governing equations (13) and retaining first order terms in ε, we get to the following linearized equations

$$
\begin{aligned}
\partial_s A^\ell - V^\ell \theta'_{\text{eq}} - \eta_\| v^\ell_\| &= 0, \\
\partial_s V^\ell + A^\ell \theta'_{\text{eq}} - 2\eta_\| v^\ell_\perp &= 0, \\
\partial_s^2 \theta^\ell - \partial_s \kappa^\ell + V^\ell &= 0, \\
\partial_t \kappa^\ell + \kappa^\ell + \chi_E(\cos \theta_{\text{eq}})\theta^\ell &= 0,
\end{aligned}
\tag{24}
$$

where

$$
\begin{aligned}
v^\ell_\| = {}& \sin \theta_{\text{eq}} \int_0^s \cos \theta_{\text{eq}} \partial_t \theta^\ell \\
& - \cos \theta_{\text{eq}} \int_0^s \sin \theta_{\text{eq}} \partial_t \theta^\ell
\end{aligned}
\tag{25}
$$

and

$$
\begin{aligned}
v^\ell_\perp = {}& \cos \theta_{\text{eq}} \int_0^s \cos \theta_{\text{eq}} \partial_t \theta^\ell \\
& + \sin \theta_{\text{eq}} \int_0^s \sin \theta_{\text{eq}} \partial_t \theta^\ell
\end{aligned}
\tag{26}
$$

are the incremental tangent and normal components of the filament's velocity, while the linearized bending moment is $M^\ell = \partial_s \theta^\ell - \kappa^\ell$. Similarly, the boundary conditions (15) become

$$
\begin{aligned}
\theta^\ell(0,t) &= 0, \\
A^\ell(1,t) = 0, \quad V^\ell(1,t) &= 0, \quad M^\ell(1,t) = 0.
\end{aligned}
\tag{27}
$$

By looking at the linear equations (24), it is worth noting that in the case of a constant equilibrium angle (see Sect. 3.1) one retrieves the model presented in [14]. However, self-weight of the filament is not accounted for in the present study and the forcing term in the evolution law for the spontaneous

curvature is modulated by $\cos\theta_{eq}$, to account for the curved equilibrium configuration of the filament. One may argue that, for given values of χ_N and $\eta_\parallel$, the stability threshold of χ_E can be estimated from the results reported in [14].

Interestingly, the system of linear, integro-differential equations (24) can be reduced to a single PDE of order 6 with the (incremental) tangential displacement as the only unknown. Similar equations arise in general from the linear analysis of elastic curved rods, as discussed in [24]. However, the numerical solution of the resulting high order PDE would require $\mathcal{C}^2$ continuity, in the case of the Finite Element Method, or the exploitation of other, more involved techniques. Furthermore, as pointed out in Fig. 3, large values of χ_E lead to equilibrium configurations in which the filament is almost straight, apart from a boundary layer at the clamp, so that the formulation of the problem in terms of the (incremental) tangential displacement may not be viable in the present context. For these reasons, we have resorted to equations (24) for the linear stability analysis of the filament's equilibrium configurations.

We now recast the linear governing equations in the following form. By removing the superscript 'ℓ' for the sake of simplicity, we define the vector of the incremental unknowns $\mathbf{X} = (A, V, \theta, \kappa)^\mathsf{T}$ and write the equations (24) in matrix form as

$$\mathbb{D}\,\partial_t \mathbf{X} = \mathbb{K}\,\mathbf{X}, \tag{28}$$

where

$$\mathbb{D} = \begin{bmatrix} 0 & 0 & \eta_\parallel J_\parallel & 0 \\ 0 & 0 & 2\eta_\parallel J_\perp & 0 \\ 0 & 0 & 0 & 0 \\ 0 & 0 & 0 & 1 \end{bmatrix} \tag{29}$$

is the *damping matrix*, with $J_\parallel$ and $J_\perp$ being the integral operators corresponding to Eqs. (25) and (26), such that $J_\parallel \partial_t \theta = v_\parallel$ and $J_\perp \partial_t \theta = v_\perp$, and

$$\mathbb{K} = \begin{bmatrix} \partial_s & -\theta'_{eq} & 0 & 0 \\ \theta'_{eq} & \partial_s & 0 & 0 \\ 0 & 1 & \partial_s^2 & -\partial_s \\ 0 & 0 & -\chi_E(\cos\theta_{eq}) & -1 \end{bmatrix} \tag{30}$$

is the *stiffness matrix*.

In order to study the stability of the equilibrium configurations, we seek for time-harmonic solutions

in the form of $\mathbf{X}(s,t) = e^{\omega t}\hat{\mathbf{X}}(s)$, such that Eq. (28) leads to the generalized eigenvalue problem

$$\omega\,\mathbb{D}\,\hat{\mathbf{X}} = \mathbb{K}\,\hat{\mathbf{X}}. \tag{31}$$

The above problem cannot be solved in closed form, so we resort to a numerical approach by means of the Finite Element Method, as discussed in Appendix B.

3.3 Results

Denoting with $\omega_{max} = \alpha + i\beta$ the eigenvalue solution of (31) with maximum real part, we distinguish between the regime of *stability* where $\alpha < 0$, and the regime of *flutter instability*, where $\alpha \geq 0$ and $\beta \neq 0$. In the regime of flutter, any perturbation of the equilibrium causes oscillations of increasing amplitude. After a transient, nonlinear effects drive the system towards a limit cycle [25], such that the transition from stability to flutter is an instance of a *supercritical Hopf bifurcation* [26].

We show in Fig. 4 the results of the stability analysis for $\chi_E \in [-50, 150]$ and $\eta_\parallel \in [0.1, 2.5]$, by comparing the results of [14], i. e. for $\chi_N = 0$, with those from our model for a small value of the natural curvature, $\chi_N = 0.01 \times 2\pi$. We notice that the behaviour of the two systems is essentially the same for $\chi_E > 0$, while they significantly differ for $\chi_E < 0$. In particular, we find that the flutter region predicted
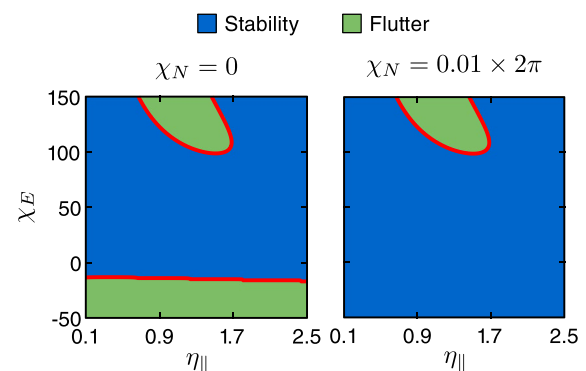
Fig. 4 Comparison between the results of the linear stability analysis for $\chi_N = 0$, i. e. the model proposed in [14] (left panel), and for $\chi_N = 0.01 \times 2\pi$ (right panel). Both panels correspond to the range of $\chi_E \in [-50, 150]$ and $\eta_\parallel \in [0.1, 2.5]$. The blue and the green regions identify the stability and flutter regimes, respectively, while the red solid lines mark the transition between the regions

by the model in [14] (left panel) is suppressed by a however small imperfection introduced by the natural curvature (right panel). We speculate that the limit for $\chi_N \to 0$ might be discontinuous and restrict any further analysis to the case of $\chi_E > 0$.

We next explore the dependence of the region of flutter instability on the model parameter χ_N. In particular, we report in Fig. 5 the results of the stability analysis for $\chi_E \in [90, 300]$, $\eta_{\parallel} \in [0.1, 2.5]$, and $\chi_N \in \{0, 8, 16, 24\} \times 2\pi$. We notice that, by increasing the value of χ_N, the critical threshold of χ_E increases for all $\eta_{\parallel}$. This is reasonable in view of the equilibrium configurations shown in Fig. 3. In fact, a larger value of χ_N entails a larger value of the external stimulus needed to completely unwind the filaments and hence a larger value of χ_E to cause flutter. Not surprisingly, our analysis predicts that only an unrolled filament (i. e. for $\chi_E > \chi_N$) may flutter.

Furthermore, the colormaps in Fig. 5 show the dependence on the relevant parameters of the oscillation frequency $\beta/2\pi$ inside the instability regions. In all panels, the frequency decreases as the value of $\eta_{\parallel}$ increases, since the latter is a dimensionless measure related to the damping of the system. Besides, fixing a pair $(\eta_{\parallel}, \chi_E)$ that falls inside the instability regions for all χ_N, we qualitatively notice that the oscillation frequency decreases for increasing χ_N.

## 4 Numerical experiments from the nonlinear model

As previously discussed, the linear stability analysis predicts the emergence of blowing-up oscillations for specific combinations of the model parameters (regime of flutter, see Sect. 3.3). We now explore the dynamics of the system after the initial transient, when nonlinear effects become prevalent. We do so by means of numerical experiments on the nonlinear model equations (13). In particular, we discretize the governing equations via the Finite Element Method; see Appendix A for details on the implementation.

An aspect of particular interest in the present investigation is the total force that the oscillating filament exerts on the surrounding fluid, and its dependence on the natural curvature χ_N. Such dynamic quantity can be easily computed by integration of Eq. (3)$_1$ and by exploiting the free-end boundary condition at $s = 1$, leading to

$$\mathbf{F}(t) := -\mathbf{C}(0, t) = \int_0^1 \mathbf{d}(s, t) \, \mathrm{d}s, \qquad (32)$$

a force, function of time, for which we denote by $\phi_{\mathbf{F}}(t)$ the angle it forms with $\mathbf{e}_2$, assumed positive if anticlockwise.

Guided by the stability analysis, we fix $\chi_E = 200$ and $\eta_{\parallel} = 1$ in the numerical simulations, such that the model parameters fall inside the flutter regions shown in Fig. 5 for all the considered values of $\chi_N = \{8, 16, 24\} \times 2\pi$ (notice the black dots in the
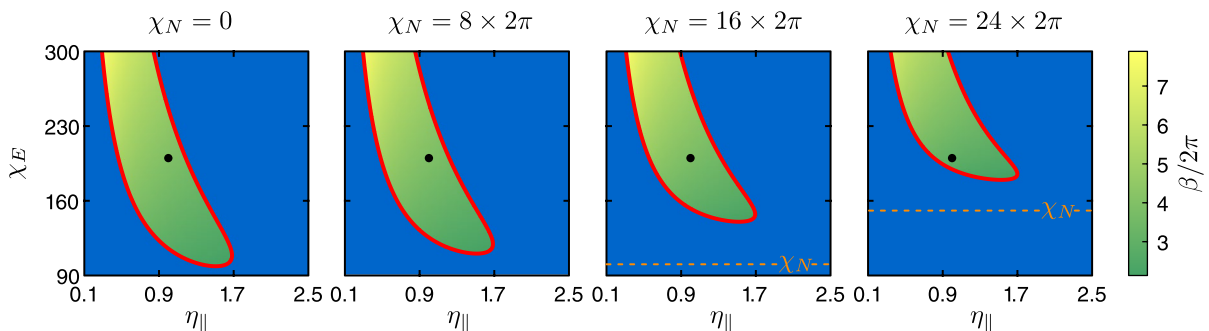
Fig. 5 Results of the linear stability analysis for $\chi_E \in [90, 300]$, $\eta_{\parallel} \in [0.1, 2.5]$, and $\chi_N \in \{0, 8, 16, 24\} \times 2\pi$. In each panel, the blue region identifies the stability regime, while the regime of flutter is inside the red solid line. The latter region is color coded according to the values of the dimensionless oscillation frequency $\beta/2\pi$. The black dots identify the pair $(\eta_{\parallel}, \chi_E) = (1, 200)$, which corresponds to the parameters fixed in Sect. 4 for the numerical simulations of the nonlinear model, while the orange dashed lines identify the value of χ_N when inside the limits of the panel
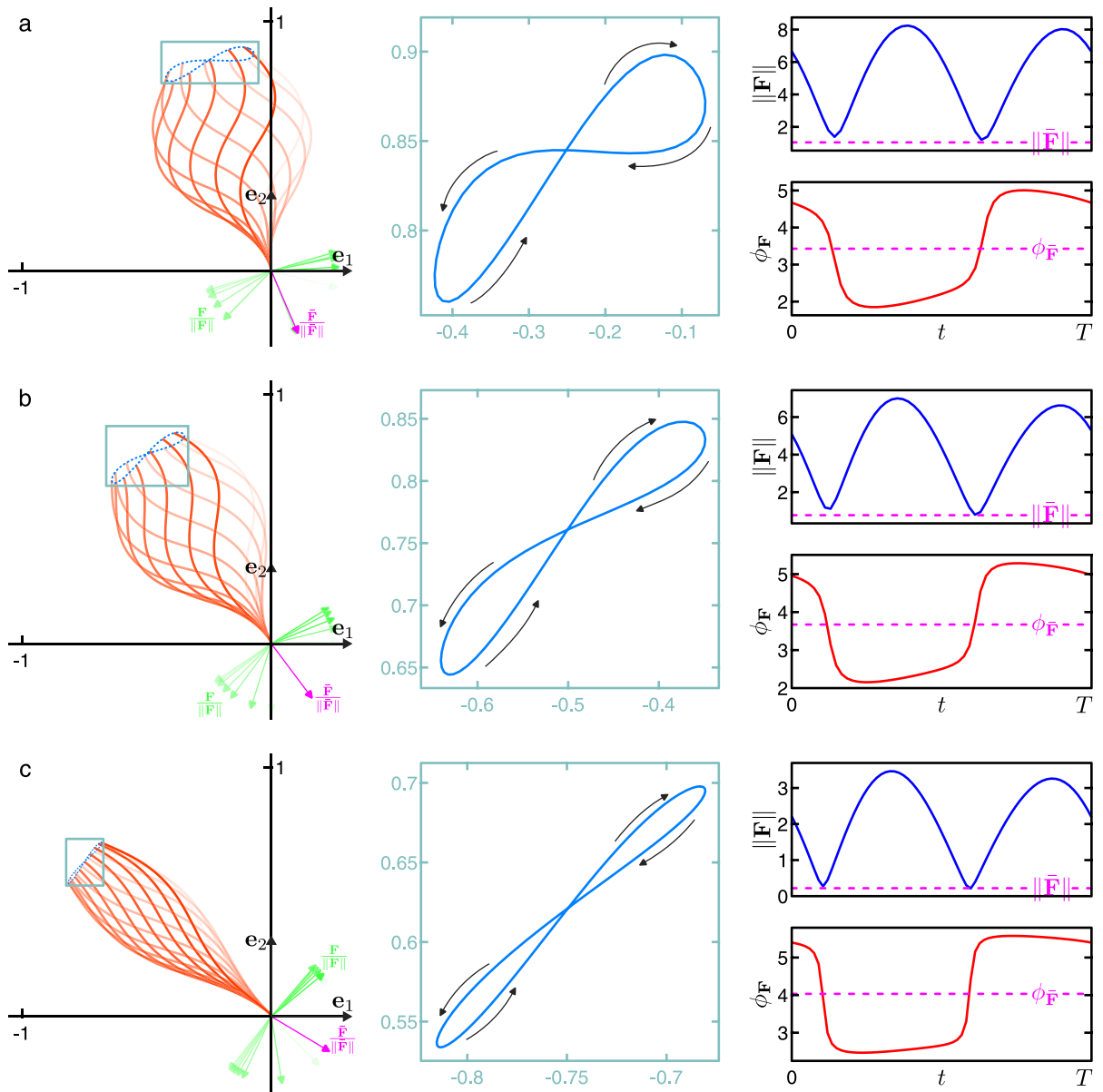
Fig. 6 Results from the numerical simulations of the nonlinear model (13) for $\chi_E = 200$ and $\eta_\parallel = 1$. The natural curvature is $\chi_N = 8 \times 2\pi$ on the top row (a), $\chi_N = 16 \times 2\pi$ on the central row (b), and $\chi_N = 24 \times 2\pi$ on the bottom row (c). In each row, the left panel shows some snapshots of the filament during a cycle. The green arrows represent the normalized reaction forces at the clamp given by Eq. (32) corresponding to the same snapshots, while the magenta arrow indicates the direction of the average force $\bar{\mathbf{F}}$, which is responsible for the net thrust of the filament. The central panel shows a closeup on the trajectory of the filament tip. The area enclosed by the orbit is a measure of the nonreciprocity of the motion. Interestingly, all points of the filament move on similar orbits. The right panel shows how the norm of the reaction force $\|\mathbf{F}(t)\|$ and the angle $\phi_{\mathbf{F}}$ evolve over a period, with the magenta dashed lines denoting the norm and direction of the averaged reaction force

figure). The results of the numerical computations are summarized in Fig. 6.

In all the cases, as predicted by the linear stability analysis, spontaneous oscillations of increasing amplitude bring the system on a closed orbit of period denoted by T. From a theoretical standpoint, such periodic solution (*limit cycle*) is attained asymptotically, but is well approximated for all practical purposes by the motion of the filament at finite time. Over one period, the reaction force at the clamp spans the cones delimited by the green arrows reported in the left panels. To quantify the net effect of this oscillating force on the fluid, we introduce $\bar{\mathbf{F}}$ as the time average of $\mathbf{F}(t)$ over one cycle of shape change, and $\phi_{\bar{\mathbf{F}}}$ the associated, positive anticlockwise angle with $\mathbf{e}_2$. While the reaction force is oriented for most of the time in a direction close to the orthogonal to the filament (graphs of $\phi_{\mathbf{F}}(t)$ on the right panels), the average force $\bar{\mathbf{F}}$, which is responsible for the net thrust exerted by the filament on the fluid, is almost aligned with the tangent to the filament (dashed lines for $\phi_{\bar{\mathbf{F}}}$ on the right panels). Its norm $\|\bar{\mathbf{F}}\|$, however, is typically much smaller than $\|\mathbf{F}(t)\|$ over a cycle.

Increasing the value of χ_N, we notice that the angle $\phi_{\bar{\mathbf{F}}}$ increases, while the amplitude of the oscillations decreases, as shown also by the tip trajectories in the central panels. It is known that the area spanned by the state variables of a system undergoing a periodic motion measures its nonreciprocity [27, 28], which in turn is linked to the norm of $\bar{\mathbf{F}}$ in our system. Indeed, a reciprocal shape change cannot generate a net thrust in the low Reynolds number regime. From the right panels of Fig. 6, we notice that the value of $\|\bar{\mathbf{F}}\|$, even if small compared to $\|\mathbf{F}(t)\|$, is not zero and decreases while increasing χ_N. We gather in Table 1 the values of the reaction force averaged over a period, showing the dependence mentioned above. We also report the values of the period T itself, showing a strong agreement with the period $2\pi/\beta$ predicted by the linear stability analysis of Fig. 5.

From the results shown in Fig. 6 and in Table 1 it is clear that it is possible to increase the horizontal component of the net thrust, for fixed $\eta_{\|}$ and χ_E, by increasing the value of the natural curvature χ_N. On the other hand, we notice that such increase in the angle $\phi_{\bar{\mathbf{F}}}$ occurs at the expense of the magnitude of the net force $\|\bar{\mathbf{F}}\|$ that the filament is able to generate. Furthermore, having in mind the evolution of the region of instability in Fig. 5, increasing χ_N too much might bring the fixed value of χ_E in the stability regime, not allowing the filament to perform self-sustained oscillations and hence generate thrust.

To further investigate the dependence of the reaction force on the natural curvature of the filament, we show in Fig. 7 the norm and the angle of $\bar{\mathbf{F}}$ as functions of $\chi_N \in [0, 200]$. These results confirm that an increase in the natural curvature leads to an increase of the angle of the net force, but to a decrease of its magnitude.

We remark a significant agreement between the angle $\phi_{\bar{\mathbf{F}}}$ and the limit angle $\theta_{\lim}$, meaning that the filament pulls indicatively along the direction to which the tip points at equilibrium. Increasing the natural curvature above the value $\chi_N \approx 164$ leads the system out of the flutter regime. Hence,

Table 1 Quantitative results of the numerical simulations shown in Fig. 6. We report the norm of the averaged reaction force on the clamp $\|\bar{\mathbf{F}}\|$ and its angle $\phi_{\bar{\mathbf{F}}}$, that correspond to the magenta dashed lines on the right panels of Fig. 6. We report also the limit angle $\theta_{\lim}$ defined in Eq. (22), the period $2\pi/\beta$ predicted by the linear stability analysis, and the actual period T of the nonlinear oscillations. All values are dimensionless
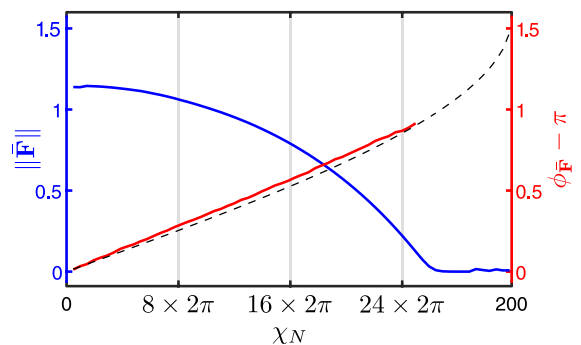
χ_N	$\|\bar{\mathbf{F}}\|$	$\phi_{\bar{\mathbf{F}}} - \pi$	$\theta_{\lim}$	$2\pi/\beta$	T
$8 \times 2\pi$	1.0938	0.2900	0.2541	0.2555	0.2500
$16 \times 2\pi$	0.8045	0.5600	0.5267	0.2754	0.2750
$24 \times 2\pi$	0.2286	0.8683	0.8541	0.3301	0.3400

Fig. 7 Plot of the averaged reaction force at the clamp $\bar{\mathbf{F}}$ as a function of $\chi_N \in [0, 200]$, keeping $\chi_E = 200$ and $\eta_{\|} = 1$ fixed. The blue solid line is the norm $\|\bar{\mathbf{F}}\|$, whereas the red solid line is the angle $\phi_{\bar{\mathbf{F}}} - \pi$, so that it is comparable with the limit angle $\theta_{\lim}$ (see Eq. (22)) reported as black dashed line. The angle $\phi_{\bar{\mathbf{F}}}$ loses significance when the force becomes zero

self-sustained oscillations disappear and the filament ceases to move the fluid and produce a net thrust.

5 Conclusions and perspectives

In this work, we have extended the model presented in [14] by endowing an active filament with a natural curvature at the fabrication stage. We have identified the different equilibrium configurations of the filament while varying the relevant model parameters. We have found that, under a minimal external stimulus of sufficiently large magnitude, a naturally curved morphoelastic filament performs nonreciprocal oscillations that break the LR symmetry while interacting with a viscous fluid. Such nonreciprocal oscillations are shown to arise as a consequence of flutter instability, in agreement with the results of [14].

For sufficiently large values of the external stimulus, the equilibrium configuration of the filament is almost straight and forms a characteristic angle with respect to the vertical direction. As flutter is initiated, oscillations of increasing amplitude take place around such equilibrium, as predicted by the linear stability analysis. Moreover, we have numerically simulated the time evolution of the system and we have shown that the periodic oscillations that arise as a consequence of the instability are nonreciprocal and allow the filament to generate a net thrust on the fluid environment. Interestingly, the direction of the thrust generated by the self-oscillating filament depends on its natural curvature. More precisely, we have shown that, fixing the value of the external stimulus, an increase in the angle at which the filament pulls on the fluid can be obtained at the expense of the magnitude of the drag force by increasing the natural curvature.

The purpose of this study is to identify suitable design principles to fabricate artificial cilia whose net effect on the fluid environment can be controlled by geometric and material parameters. In this respect, an interesting application of our results may be the study of the collective behaviour of artificial ciliary carpets, in which each cilium can be properly engineered so as to have different natural curvature and generate thrust at different angles, while fluttering under the same constant and uniform external

stimulus. Lastly, it would be interesting to investigate formulations of the linear stability analysis alternative to that presented in Sect. 3.2.

Data availibility statement The authors declare that the data supporting the findings of this study are available within the paper.

Appendix

A Details on the numerical simulations

All numerical experiments were performed by Finite Element simulations using the commercial software COMSOL Multiphysics® 6.1 (build 357).

The balance of linear momentum in the form of Eq. $(3)_1$, along with the zero force boundary condition at the endpoint $s = 1$, allows to compute the contact forces as

$$\mathbf{C}(s, t) = \int_s^1 \mathbf{d}(\sigma, t) \, \mathrm{d}\sigma, \tag{A1}$$

where $\mathbf{C}$ and $\mathbf{d}$ are dimensionless.

For the formulation of the Finite Element model, the two remaining equations, namely the balance of angular momentum and the evolution law of the spontaneous curvature, were recast in weak form. Starting with the balance of angular momentum, we multiply $(13)_3$ by a suitable test function $\hat{\theta}$ and apply integration by parts; exploiting the zero moment boundary condition $(15)_4$, we arrive at the following equation for the unknown θ

$$\int_0^1 \left[(\partial_s \theta - \kappa - \chi_N) \partial_s \hat{\theta} - V\hat{\theta} \right] \mathrm{d}s = 0. \tag{A2}$$

Similarly, testing Eq. (13)$_4$ by a suitable function $\hat{\kappa}$, we obtain the weak form for the evolution of the spontaneous curvature:

$$\int_0^1 \left[\left(\partial_t \kappa + \kappa + \chi_E \sin\theta \right) \hat{\kappa} \right] ds = 0. \qquad (A3)$$

The parametrization interval [0, 1] was decomposed with a nonuniform mesh of 60 elements, which was finer near the clamp in order to better represent the boundary layer of some equilibrium solutions discussed in Sect. 3.1. For the semi-discretization in space, θ and κ were approximated by quadratic and by linear Lagrange polynomials, respectively.

The temporal discretization was performed by backward finite differences using using the Time Dependent Solver of COMSOL with a step size $\Delta t = 0.005$.

A.1 Reconstruction of velocity field in the fluid

Having numerically solved the nonlinear governing equations for the configuration of the filament and for the distribution of the drag forces acting upon it, one can reconstruct the velocity field induced in the surrounding fluid (shown in Fig. 1) by the motion of the filament via a boundary integral approach, as detailed in the following.

Let us recall the fundamental solution of the Stokes equations associated with a point force $\mathbf{f} \in \mathbb{R}^2$: the so-called *Stokeslet*. It is known [29] that the velocity field induced in a viscous fluid by a point force $\delta(\boldsymbol{\xi})\mathbf{f}$ concentrated at $\boldsymbol{\xi} \in \mathbb{R}^2$ is given by

$$\mathbf{u}(\mathbf{x}) = \frac{1}{8\pi\mu} \mathbb{G}(\mathbf{x};\boldsymbol{\xi})\mathbf{f}, \qquad (A4)$$

where $\mathbf{x} \in \mathbb{R}^2$, μ is the viscosity of the fluid, and the *Oseen tensor* $\mathbb{G}$ reads

$$\mathbb{G}(\mathbf{x};\boldsymbol{\xi}) = \frac{1}{R}\mathbb{I} + \frac{1}{R^3}\mathbf{R} \otimes \mathbf{R}, \qquad (A5)$$

with $\mathbf{R} = \mathbf{x} - \boldsymbol{\xi}$ and $R = \|\mathbf{R}\|$. By exploiting such fundamental solution, the effect of the filament on the surrounding fluid can be approximated through the drag force distribution $-\mathbf{d}(s)$ in Eq. (4), so that at any place $\mathbf{x}$ not on the filament the velocity reads

$$\mathbf{u}(\mathbf{x}) = -\frac{1}{8\pi\mu} \int_0^L \mathbb{G}(\mathbf{x};\mathbf{r}(s))\mathbf{d}(s)\,ds. \qquad (A6)$$

This approximation, valid again in the slender limit, is only local as hydrodynamic self-interactions of the filament are not considered.

From this approximation of the velocity field at all points in the fluid domain, we can compute *path lines*, that are the trajectories of tracer particles in Fig. 1, as solutions of the differential equation

$$\dot{\mathbf{x}}(t) = \mathbf{u}(\mathbf{x}(t), t). \qquad (A7)$$

The numerical solution of this equation was obtained using MATLAB's ode113 solver.

A.2 Parameters for the simulations in Fig. 1

The results in Fig. 1 were obtained by simulations of the nonlinear equations in nondimensional form (13), as detailed in the previous sections of this Appendix. The nondimensional parameters were set as follows: $\eta_\parallel = 1$, $\chi_E = 200$ and $\chi_N = 24 \times 2\pi$. For the central panel, the electric field was rotated by an angle 0.8541, corresponding to the limit equilibrium angle (22) of the filament with natural curvature in the right panel for the selected parameters.

B Numerical solution of the generalized eigenvalue problem

In this section we give some details on the approximation of the generalized eigenvalue problem (31) implemented in COMSOL Multiphysics® 6.1.

The internal forces were computed by integration of the drag distribution on the filament, as in (A1). However, in the linear case the drag distribution is computed with the linear counterparts of the velocity components (25) and (26).

Equations (24)$_3$ and (24)$_4$ were rewritten in weak form and discretized as their nonlinear counterparts as discussed in Appendix A.

With this semi-discretization in space, the damping and stiffness matrices can be assembled, leading to the generalized eigenvalue problem

$$\omega \mathbb{D}_h \hat{\mathbf{X}}_h = \mathbb{K}_h \hat{\mathbf{X}}_h, \qquad (B8)$$

where $\mathbf{X}_h$ is the vector of nodal unknowns and $\mathbb{D}_h$ and $\mathbb{K}_h$ are the discrete damping and stiffness matrices, respectively. Once the discrete system (B8) has been assembled, the eigenvalues and eigenfunctions are determined by the solver using the QZ algorithm [30].

We remark that computing the internal actions as (A1) instead of imposing their balance in weak form removes empty columns in the discrete damping matrix. These empty columns are caused by the absence of time derivatives of A^ℓ and V^ℓ in the balance Eq. (24) and can compromise the reliability of the eigenvalue solver. The weak balance Eq. (A2) does not contain time derivatives explicitly, but the integral formulation of V^ℓ does contain time-derivatives of θ^ℓ, through the velocity components in Eqs. (25) and (26).

References

1. Ferreira R, Fukui H, Chow R, Vilfan A, Vermot J (2019) The cilium as a force sensor: myth versus reality. J Cell Sci 132(14):213496. https://doi.org/10.1242/jcs.213496
2. Tamm SL (1972) Ciliary motion in paramecium. J Cell Biol 55(1):250–255. https://doi.org/10.1083/jcb.55.1.250
3. Lauga E (2020) The fluid dynamics of cell motility. Cambridge texts in applied mathematics. Cambridge University Press, Cambridge. https://doi.org/10.1017/97813 16796047
4. Shapiro OH, Fernandez VI, Garren M, Guasto JS, Deballon-Vesque FP, Kramarsky-Winter E, Vardi A, Stocker R (2014) Vortical ciliary flows actively enhance mass transport in reef corals. Proc Natl Acad Sci 111(37):13391–13396. https://doi.org/10.1073/pnas.1323094111
5. Yuan S, Wang Z, Peng H, Ward SM, Hennig GW, Zheng H, Yan W (2021) Oviductal motile cilia are essential for oocyte pickup but dispensable for sperm and embryo transport. Proc Natl Acad Sci 118(22):2102940118. https://doi.org/10.1073/pnas.2102940118
6. Lin J, Nicastro D (2018) Asymmetric distribution and spatial switching of dynein activity generates ciliary motility. Science 360(6387):1968. https://doi.org/10.1126/science.aar1968
7. Oosten CL, Bastiaansen CWM, Broer DJ (2009) Printed artificial cilia from liquid-crystal network actuators modularly driven by light. Nat Mater 8(8):677–682. https://doi.org/10.1038/nmat2487
8. Kwon GH, Park JY, Kim JY, Frisk ML, Beebe DJ, Lee S (2008) Biomimetic soft multifunctional miniature aquabots. Small 4(12):2148–2153. https://doi.org/10.1002/smll.200800315
9. Kaynak M, Ozcelik A, Nama N, Nourhani A, Lammert PE, Crespi VH, Huang TJ (2016) Acoustofluidic actuation of in situ fabricated microrotors. Lab Chip 16(18):3532–3537. https://doi.org/10.1039/c6lc00443a
10. Dong X, Lum GZ, Hu W, Zhang R, Ren Z, Onck PR, Sitti M (2020) Bioinspired cilia arrays with programmable nonreciprocal motion and metachronal coordination. Sci Adv. https://doi.org/10.1126/sciadv.abc9323
11. Miao J, Zhang T, Li G, Shang W, Shen Y (2021) Magnetic artificial cilia carpets for transport, mixing, and directional diffusion. Adv Eng Mater. https://doi.org/10.1002/adem.202101399
12. Han E, Zhu L, Shaevitz JW, Stone HA (2021) Low-Reynolds-number, biflagellated Quincke swimmers with multiple forms of motion. Proc Natl Acad Sci 118(29):2022000118. https://doi.org/10.1073/pnas.2022000118
13. Korner K, Kuenstler AS, Hayward RC, Audoly B, Bhattacharya K (2020) A nonlinear beam model of photomotile structures. Proc Natl Acad Sci 117(18):9762–9770. https://doi.org/10.1073/pnas.1915374117
14. Cicconofri G, Damioli V, Noselli G (2023) Nonreciprocal oscillations of polyelectrolyte gel filaments subject to a steady and uniform electric field. J Mech Phys Solids 173:105225. https://doi.org/10.1016/j.jmps.2023.105225
15. Camalet S, Jülicher F (2000) Generic aspects of axonemal beating. New J Phys 2(1):324. https://doi.org/10.1088/1367-2630/2/1/324
16. Bayly PV, Dutcher SK (2016) Steady dynein forces induce flutter instability and propagating waves in mathematical models of flagella. J R Soc Interface 13(123):20160523. https://doi.org/10.1098/rsif.2016.0523
17. Agostinelli D, Lucantonio A, Noselli G, DeSimone A (2020) Nutations in growing plant shoots: the role of elastic deformations due to gravity loading. J Mech Phys Solids 136:103702. https://doi.org/10.1016/j.jmps.2019.103702
18. Agostinelli D, DeSimone A, Noselli G (2021) Nutations in plant shoots: endogenous and exogenous factors in the presence of mechanical deformations. Front Plant Sci. https://doi.org/10.3389/fpls.2021.608005
19. Agostinelli D, Noselli G, DeSimone A (2021) Nutations in growing plant shoots as a morphoelastic flutter instability. Philos Trans R Soc A Math Phys Eng Sci 379:20200116. https://doi.org/10.1098/rsta.2020.0116

20. Hirokawa N, Okada Y, Tanaka Y (2009) Fluid dynamic mechanism responsible for breaking the left-right symmetry of the human body: the nodal flow. Annu Rev Fluid Mech 41(1):53–72. https://doi.org/10.1146/annurev.fluid.010908.165141

21. Antman SS (2005) Nonlinear problems of elasticity. Applied mathematical sciences, vol 107, 2nd edn. Springer, New York

22. Goriely A (2017) The mathematics and mechanics of biological growth. Interdisciplinary applied mathematics, vol 45. Springer, New York. https://doi.org/10.1007/978-0-387-87710-5

23. Chauvet H, Moulia B, Legué V, Forterre Y, Pouliquen O (2019) Revealing the hierarchy of processes and timescales that control the tropic response of shoots to gravistimulations. J Exp Bot 70(6):1955–1967. https://doi.org/10.1093/jxb/erz027

24. Lamb H (1887) On the flexure and the vibrations of a curved bar. Proc Lond Math Soc 19(1):365–377. https://doi.org/10.1112/plms/s1-19.1.365

25. Bigoni D, Dal Corso F, Kirillov ON, Misseroni D, Noselli G, Piccolroaz A (2023) Flutter instability in solids and structures, with a view on biomechanics and metamaterials. Proc R Soc A 479(2279):20230523. https://doi.org/10.1098/rspa.2023.0523

26. Strogatz S (2019) Nonlinear dynamics and chaos, 2nd edn. CRC Press, Boca Raton

27. Golestanian R, Ajdari A (2008) Analytic results for the three-sphere swimmer at low reynolds number. Phys Rev E 77(3):036308. https://doi.org/10.1103/physreve.77.036308

28. Khaderi SN, Baltussen MGHM, Anderson PD, Ioan D, Toonder JMJ, Onck PR (2009) Nature-inspired microfluidic propulsion using magnetic actuation. Phys Rev E 79(4):046304. https://doi.org/10.1103/physreve.79.046304

29. Kim S, Karrila SJ (2005) Microhydrodynamics: principles and selected applications. Butterworth-Heinemann series in chemical engineering. Dover Publications, Stoneham

30. Moler CB, Stewart GW (1973) An algorithm for generalized matrix eigenvalue problems. SIAM J Numer Anal 10(2):241–256